Chemical Engineering Journal 513 (2025) 162838

Contents lists available at ScienceDirect

Chemical Engineering Journal

journal homepage: www.elsevier.com/locate/cej

Hydrogel-Encapsulated phase change materials for Enhanced heat storage and water evaporation efficiency

Casey Onggowarsito [a], Stella Zhang [a], Yihan Shi [a], Shudi Mao [a], An Feng [a], Gabriela Martins [a], Zeyu Shao [b], Edgar H.H. Wong [b], Wenshan Guo [a,*], Qiang Fu [a,*]

[a] Centre for Technology in Water and Wastewater, School of Civil and Environmental Engineering, University of Technology Sydney, Ultimo 2007 NSW, Australia
[b] Centre for Advanced Macromolecular Design (CAMD) and Australian Centre for NanoMedicine (ACN), School of Chemical Engineering, UNSW Australia, Sydney, NSW 2052 Australia

ARTICLE INFO

Keywords:
Solar steam generation (SSG)
Dual layer hydrogel (DLH)
Phase change material (PCM)
Heat storage
Desalination

ABSTRACT

The solar steam generation (SSG) system is a promising, sustainable, and environmentally friendly technology that has garnered significant attention for its ability to produce freshwater using sunlight as a renewable energy source. However, solar energy is inherently intermittent, as its utilization depends on factors such as time of day and weather conditions, with daytime cloud cover often reducing sunlight intensity and compromising evaporation performance. To address this, we incorporated both hydrophilic and hydrophobic phase-change materials (PCMs) into the top layer of a dual-layer hydrogel (DLH) SSG to enhance heat management. Under solar irradiation, the top evaporating layer generates significant heat, rapidly elevating the surface temperature while the phase change material (PCM) concurrently stores thermal energy. During periods of interrupted solar exposure, the PCM releases stored heat, ensuring continuous water evaporation in the DLH SSG. The system achieved an evaporation rate of 3.52 kg $m^{-2}h^{-1}$ under one-sun irradiation, corresponding to an efficiency of 83 %, and sustained an evaporation rate of 26 g m^{-2} min^{-1} of lightless operation. Furthermore, the DLH SSG system facilitates salt removal and sterilization via the bottom layer that contained positively charged polymers, thereby offering an effective and practical approach to seawater desalination or lake water treatment to address critical water scarcity challenges.

1. Introduction

Our ongoing water crisis presents a persistent challenge primarily driven by the steadily increasing demand for water. This annual growth of approximately 1 % in water demand can be attributed to the growing needs in various economic sectors, including industrial manufacturing, power generation, agricultural, and domestic use. Our current water production system may not provide a sustainable solution in the long term due to its high operational costs, harmful by-products, and thermodynamic limitations [1–3].

A greener alternative water production system known as solar steam generation (SSG) has captured significant attention due to its promising potential for sustainable water production and filtration. SSG utilizes renewable solar energy to distill contaminated water through heat generated by photothermal materials (PTMs) such as plasmonic nanoparticles, semiconductors, conjugated polymers, and carbon materials [4–6]. The reinvention of the SSG evaporation strategy from volumetric to interfacial evaporation has enabled more efficient evaporation by localizing heat production and conversion at the evaporation interface, thereby minimizing conductive heat loss to the bulk water [7].

Despite this, current interfacial SSG systems continue to face challenges in heat management. A significant issue is the considerable heat loss to the surrounding environment through convection and radiation, leading to an inefficient water production rate [8,9]. There have been many methods of suppressing heat loss in SSG systems. For example, incorporating low thermal conductive materials or insulators as the base of interfacial SSGs is a simple approach to minimize heat loss to bulk water [10,11]. Another strategy involves using Janus SSGs with a hydrophilic bottom layer and a hydrophobic top layer, effectively reducing heat loss by limiting the evaporator's exposure to bulk water [12,13]. Furthermore, solar itself is characterized by intermittency, and its utilization efficiency is influenced by factors such as the time of day and

* Corresponding authors at: Centre for Technology in Water and Wastewater, School of Civil and Environmental Engineering, University of Technology Sydney, Ultimo 2007, NSW, Australia (W. Guo).
E-mail addresses: wguo@uts.edu.au (W. Guo), Qiang.Fu@uts.edu.au (Q. Fu).

https://doi.org/10.1016/j.cej.2025.162838
Received 10 January 2025; Received in revised form 4 April 2025; Accepted 18 April 2025
Available online 19 April 2025

weather conditions. For instance, clouds during the day can temporarily reduce sunlight intensity, directly impacting the photothermal conversion and, consequently, the water evaporation performance of SSGs. Fluctuations in solar irradiance can lead to thermal instability, highlighting the need for innovative strategies to store and manage thermal energy, ensuring stable performance even during periods of reduced solar input.

To address these challenges, this study aims to develop a cost-effective, dual-layer hydrogel-based SSG system integrated with phase-change materials (PCMs) to enhance heat retention and maintain stable water evaporation rate under varying solar conditions. Additionally, the study seeks to evaluate the system's scalability and effectiveness for practical desalination and water purification applications.

Phase-change materials (PCMs) are widely utilized in building applications and battery thermal management systems due to their phase-transition nature of storing and releasing latent heat energy [14–17]. The incorporation of PCM in an SSG system potentially allows for excess heat storage produced by PTM's light conversion, generating consistent surface temperature under the absence of light. However, PCM encapsulation within porous materials tend to contain leakage issue due to PCM's volume expansion during its solid to liquid phase transition [18]. In this study, we developed cost-effective, PCM containing dual layer hydrogels (denoted as DLHPCMs) by incorporating PTM and hydrophilic PCM polyethylene glycol (PEG1500) or hydrophobic PCM docosane PCM into the top layer of the DLH using copolymerization and vacuum encapsulation strategies. This strategy allows both hydrophilic and hydrophobic PCMs to be encapsulated within a porous DLH hydrogel, resulting in excess heat energy generated by the PTMs to be stored in the DLH SSG material through the PCM, effectively reducing heat loss. It was demonstrated that, due to the heat storage property of the PCM, the surface temperature of the DLHPCM increased, achieving a water evaporation rate of 3.52 kg $m^{-2}h^{-1}$ under sunlight irradiation. In the absence of solar irradiation, the PCM released the stored heat in 20 min, maintaining an evaporation rate of 0.51 kg m^{-2}. Moreover, DLHPCM exhibited stable performance in desalination and lake-water filtration, effectively removing over 99.9 % of metal ions and bacteria from local seawater and lake-water sources. Additionally, its scalability was demonstrated through outdoor seawater desalination tests, yielding a water output of 12.38 L m^{-2} day^{-1}. This result thus underscores its potential for large-scale clean water harvesting applications in the future.

2. Experimental

2.1. Materials

All reagents including polyvinyl alcohol (PVA, M_w: 89 – 98 kDa), [2-(acryloyloxy)ethytrimethyl ammonium chloride (AETAC, 80 wt% in H_2O), *N,N'*-methylenebis(acrylamide) (BIS, 99 %), *N,N,N',N'*-tetramethyl ethylenediamine (TEMED, 99 % aqueous solution), ammonium persulfate (APS), glutaraldehyde (GA, 25 % aqueous solution), graphene oxide (GO), polyethylene glycol (PEG1500, M_w: 1,500 Da), and docosane (99 %) were purchased from Sigma-Aldrich and used without further purification.

2.2. The synthesis of dual-layer hydrogel (DLH)

The bottom layer of DLH was synthesized by adding, mixing, and sonicating 44.2 mg BIS crosslinker, 0.6 mL AETAC monomer, 10 mL 10 wt% PVA solution, and 75 μL TEMED catalyst. The evenly mixed solution was then added with 1 mL of 100 mg mL^{-1} APS initiator to solidify the mixture and form the bottom layer. Subsequently, a solution containing 5 mL 10 wt% PVA solution and 5 mL of 1 mg mL^{-1} GO solution was evenly mixed and placed on top of the solidified DLH's bottom layer. The mixture solution was then added with 125 μL of 25 wt% GA crosslinker, followed by 250 μL 1 M HCl drop-wise. The mixture was then gently stirred for the solution to evenly mixed, and left under room temperature for the solution to solidify, affording the top layer. The prepared DLH was then frozen overnight at −20 °C and frozen dried for approximately 48 h.

2.3. The synthesis of dual-layer hydrogel containing phase change material (DLHPCM)

DLHPCM-Docosane hydrogels were synthesized by melting specific amounts of docosane by heating it above 50 °C for approximately 10 min. The prepared DLH hydrogels were then placed in a vacuum oven at 70 °C and 1 bar of pressure, where they were exposed to 1, 2, and 3 g of docosane until all PCM was absorbed, resulting in the formation of DLHPCM1g, DLHPCM2g, and DLHPCM3g respectively.

DLHPCM-PEG1500 hydrogels were synthesized by mixing 5 mL 10 wt% PVA solution, 5 mL of 1 mg mL^{-1} GO solution, and 1 g PEG1500 PCM. The mixture was heated to 90 °C and stirred at 1000 rpm to fully melt and blend the PCM within the mixture. After an hour, various amounts of GA crosslinker and 250 μL of 1 M HCl catalyst were added to the blended mixture. The mixture was then shaken gently and left at room temperature to form the top layers. Thereafter, a mixture solution containing BIS, AETAC, PVA and EMED, and APS was added and solidified using 1 mL of 100mgmL^{-1} APS at room temperature. Once the mixture is crosslinked, the prepared DLHPCM was frozen overnight to then be frozen-dried for 48 h. The prepared DLHCPMs containing 125, 250, and 375 μL GA crosslinker are denoted as DLHPCM125, DLHPCM250, and DLHPCM375, respectively.

2.4. Characterization

Scanning electron microscope (SEM) imaging of all hydrogels was captured by Zeiss Supra 55VP. Fourier-Transform Infrared (FTIR) spectroscopy SHIMADZU MIRacle 10 single reflection ATR accessory was used to confirm the chemical composition of all hydrogels. The light absorption property of hydrogels was observed using Cary 7000 Universal Measurement ultraviolet–visible-near infrared (UV–VIS-NIR) spectrophotometer between the range 350 – 2500 nm. The vaporization enthalpies and charge discharge property were measured using NETZSCH Differential Scanning Calorimetry (DSC) 300 Caliris. Filtered water obtained from water filtration of seawater and lake water was analayzed by Agilent 7900 Inductively Coupled Plasma Mass Spectrometry (ICP-MS).

2.5. Indoor solar steam generation

Water evaporation performance and water filtration tests were conducted under an inhouse built cabinet box using a laboratory solar light simulator (NBeT HSX-F3000) xenon light source, adjusted, and calibrated to one sun irradiation ($\leq$1 kW m^{-2}). The solar light simulator was turned on for approximately 20 min prior to the water evaporation testing to stabilize and equilibrate with the surrounding environment. Water evaporation mass loss was measured sequentially every 4 min for 1 h cycle using an analytical mass balance (OHAUS Pioneer IC-PX124). The surface temperature of each hydrogel was captured and recorded using a thermal camera (Fluke PTi120) for every 5 min. The collected filtered water was obtained via a glass jar to be ICP-MS.

2.6. Outdoor solar steam generation

The outdoor solar steam generation (SSG) test was conducted using a custom-built device designed to evaluate the performance of hydrogel scaling for water production and vapor collection. The setup features two TEC1-12706 thermoelectric (TE) modules water-cooling condenser that utilized pumped recycled seawater to create a cold air environment within the evaporation chamber. This cold air was injected into the chamber using two 60x60 mm, 15 V cooling fans. Both the water pump

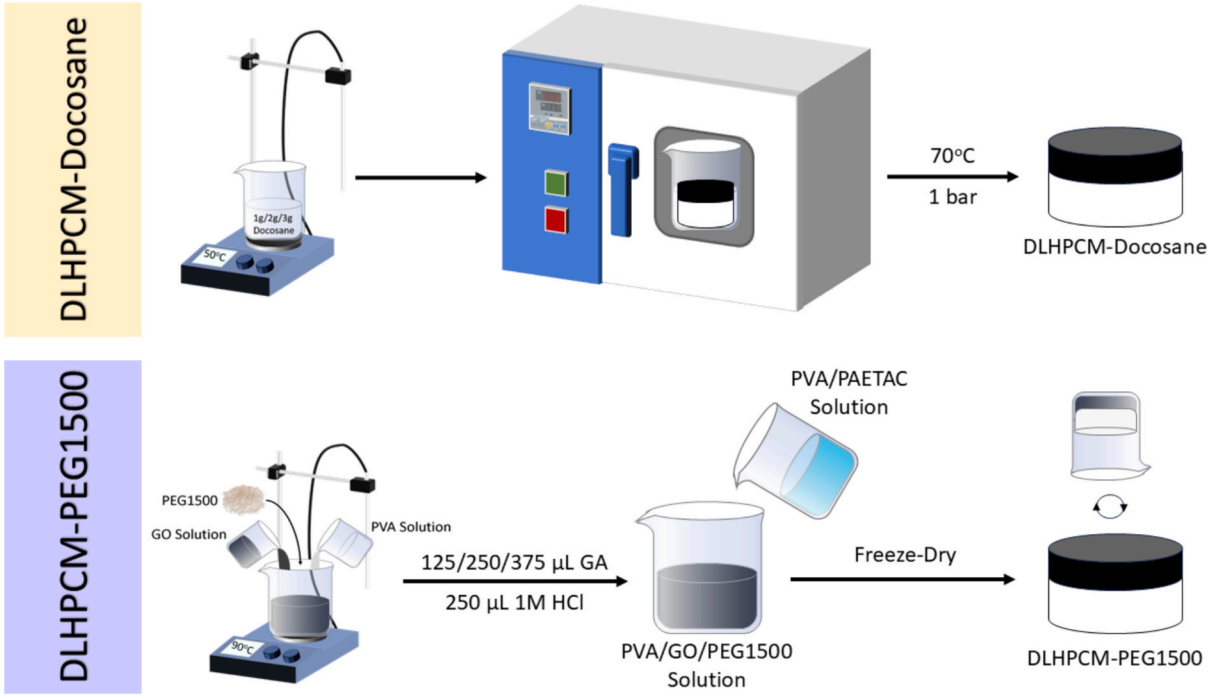

Fig. 1. Schematic of DLHPCM-Docosane and DLHPCM-PEG1500 synthesis.

and cooling fans were powered by a Rovin 300 W portable power station, recharged via a 12 V 10 W portable solar panel. Temperature and solar irradiation were monitored and recorded approximately every 30 min from 8.30 AM to 5.30 PM. The filtered seawater collected during the experiment was measured to assess the water production performance.

2.7. Anti-bacterial study

The bactericidal efficiency of the hydrogel was evaluated against Gram-positive pathogen *S. Aureus* ATCC 29213. Hydrogel samples were sectioned into small pieces, immersed in PBS for 24 h, and allowed to fully swell, reaching a mass of ca. 70 mg. The swollen hydrogel samples were then transferred to a 24-well microplate (Costar, Corning). Separately, a single bacterial colony was cultured in 10 mL of Mueller-Hinton Broth (MHB) at 37 °C with 180 rpm shaking overnight. The overnight culture was diluted in phosphate-buffered saline (PBS) such that the bacteria concentration was ca. 10^7 CFU mL^{-1} for the killing study. The bacterial suspension was then added into the wells containing the hydrogel samples (ca. 1 mL bacteria suspension per 100 mg swollen hydrogel). A negative control, consisting solely of the bacterial

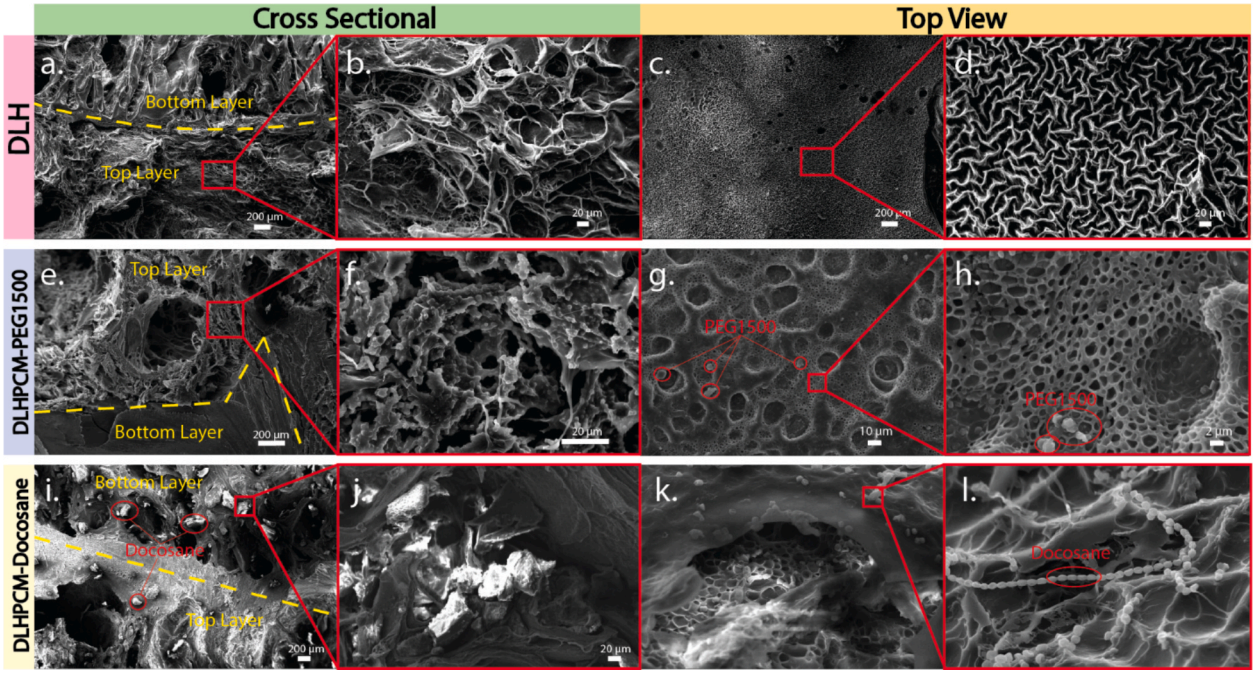

Fig. 2. Scanning electron microscope (SEM) cross-sectional images of DLH (a, b), DLHPCM-PEG1500 (e, f), and DLHPCM-Docosane (i, j), as well as evaporative surface images of DLH (c, d), DLHPCM-PEG1500 (g, h), and DLHPCM-Docosane (k, l).

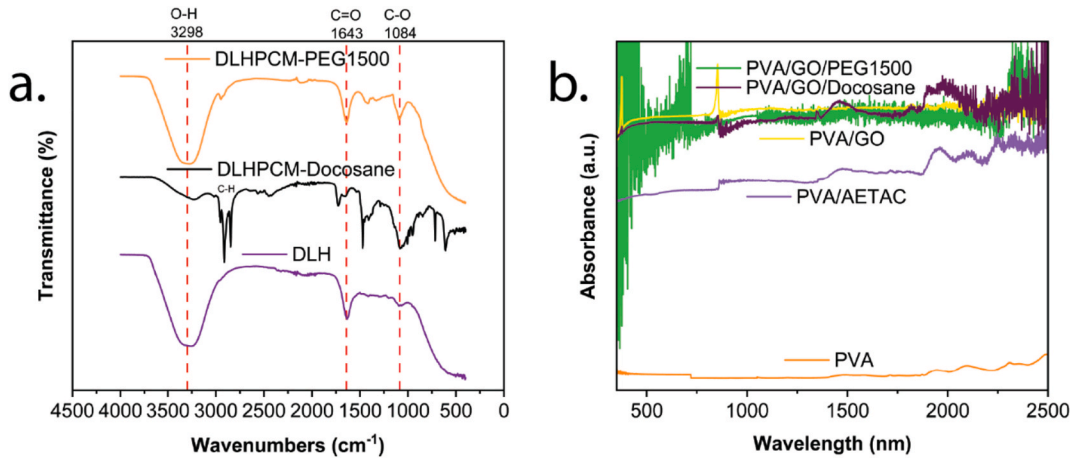

Fig. 3. (a) Fourier-Transform Infrared (FTIR) and (b) ultraviolet–visible-near infrared (UV–VIS-NIR) spectra showing the chemical composition and light absorption ability of the hydrogels, respectively.

suspension without hydrogel, was also included. The microplate was incubated at 37 °C for 24 h, after which the samples were subjected to ultrasonication (150 W, 40 kHz, Australia) for 10 min. The viability of planktonic cells in each well was then determined by a drop plate method where the planktonic cells were serially diluted in PBS and plated onto Luria Bertani agar. After 24 h incubation at 37 °C, the bacteria colonies were counted and CFU analysis was performed. Each assay was performed in duplicate and repeated in two independent trials.

3. Results and discussion

3.1. Preparation and characterization of DLHPCMs

In this study, novel double-layered hydrogels (DLHs) incorporating hydrophobic or hydrophilic phase change materials (PCMs) were synthesized, alongside a bare DLH without PCM for comparison. The bottom water-absorbent layer of all samples was formulated using polyvinyl alcohol (PVA) and poly[2-(acryloyloxy)ethytrimethyl ammonium chloride] (PAETAC) to optimize water absorption and mechanical properties. The top layers consisted of PVA and graphene oxide (GO), with chemical bonding between the bottom and top layers were achieved through the reaction between the hydroxyl (–OH) groups of PVA and aldehyde (–CHO) groups of glutaraldehyde (GA), as shown in Fig. 1.

Hydrophobic docosane and hydrophilic polyethylene glycol 1500 (PEG1500) PCMs were encapsulated within the top layer to create DLHPCMs. For docosane, pristine DLHs were immersed in melted docosane at varying concentrations (1, 2, and 3 g) under vacuum conditions, resulting in DLHPCM-Docosane samples designated as DLHPCM1g, DLHPCM2g, and DLHPCM3g, respectively. The encapsulation process revealed that the hydrogel, with an average mass of 2 g after freeze drying, could effectively incorporate up to 3 g of docosane. However, beyond this threshold, the absorption rate of melted docosane significantly declined, and leakage of encapsulated docosane was observed.

A customized DLHPCM-PEG1500 hydrogel was synthesized using a top-down approach to address the coagulation tendency of PEG1500 during cooling, differing from conventional DLHs. The top layer was prepared by mixing PEG1500, PVA, and GO, followed by heating and continuous stirring to ensure uniform heat distribution and prevent coagulation. After introducing the crosslinker and catalyst, the solution was allowed to cool at room temperature, facilitating hydrogel formation. Subsequently, the bottom layer, consisting of the same PVA and PAETAC composition, was prepared and layered onto the previously gelled top layer. In contrast, PEG1500 loading was restricted to 1 g due to pronounced coagulation with PVA at higher mass loading. This limitation arises from the encapsulation mechanism of PEG1500, where increased mass loadings exacerbate its tendency to copolymerize with PVA [19,20], leading to the formation of micelle-like particles at elevated temperatures.

As shown in Fig. 2, the microstructures of the DLHPCMs (Fig. 2**e** and **i**) exhibit a well-integrated bilayer architecture, analogous to the structure observed in pristine DLHs (Fig. 2**a**). This structural coherence is attributed to the incorporation of PVA in both the top and bottom layers, enhancing interlayer compatibility. Cross-sectional SEM images of all hydrogels (Fig. 2**b, f**, and **j**) reveal a combination of micro- and macroporous structures, which promote efficient water transport within the hydrogel matrix.

The upper layers of the DLHPCM-PEG1500 (Fig. 2**f**) and DLHPCM-Docosane (Fig. 2**j**) demonstrate successful encapsulation of the respective PCMs, as evidenced by distinct PCM particles embedded within the matrix. Top-view SEM images reveal high surface roughness across the evaporative surface of all hydrogels, a feature that enhances light absorption properties consistent with previous studies [2].

Notably, the encapsulation of both hydrophilic PEG1500 and hydrophobic docosane partially obstructed water transport pathways by covering the large pores in the hydrogels. In addition, the DLHPCM-Docosane hydrogel displayed a significantly reduced porous structure (Fig. 2**j** – **l**). Consequently, water evaporation in the DLHPCM-Docosane hydrogel is confined to small openings on the surface, as depicted in Fig. 2**k**. In contrast, the encapsulation of hydrophilic PEG1500 did not exhibit this limitation, preserving open water transport pathways throughout the hydrogel structure.

The presence of PVA, PAETAC, and GO within all three types of hydrogels was confirmed by the FTIR spectra analysis (Fig. 3**a**). The characteristic peaks corresponding to DLH's O-H, C=O, and C-O vibrational stretching were observed at 3298, 1646, and 1084 cm^{-1} respectively, consistent with previous reports [21–23]. The successful encapsulation of docosane within the DLH hydrogel was verified by the presence of broad C-H vibrational peaks, with sub-peaks identified at 2952, 2913, and 2847 cm^{-1} [24]. In contrast, the encapsulation of PEG1500 was more challenging to confirm via FTIR due to its overlapping functional groups with PVA, PAETAC and GO, such as the broad O-H and C-O stretching at 3298 and 1084 cm^{-1} [25]. However, besides SEM, the presence of PEG1500 was further corroborated by DSC signals of DLHPCM125, 250, and 375 as discussed below. Moreover, the top layers of all hydrogels exhibited broad light absorption across the UV–VIS-NIR range, effectively converting absorbed electromagnetic wave into heat, as demonstrated by the UV spectra presented in Fig. 3**b**.

PEG1500, docosane, and DLHPCM unsaturated hydrogels were

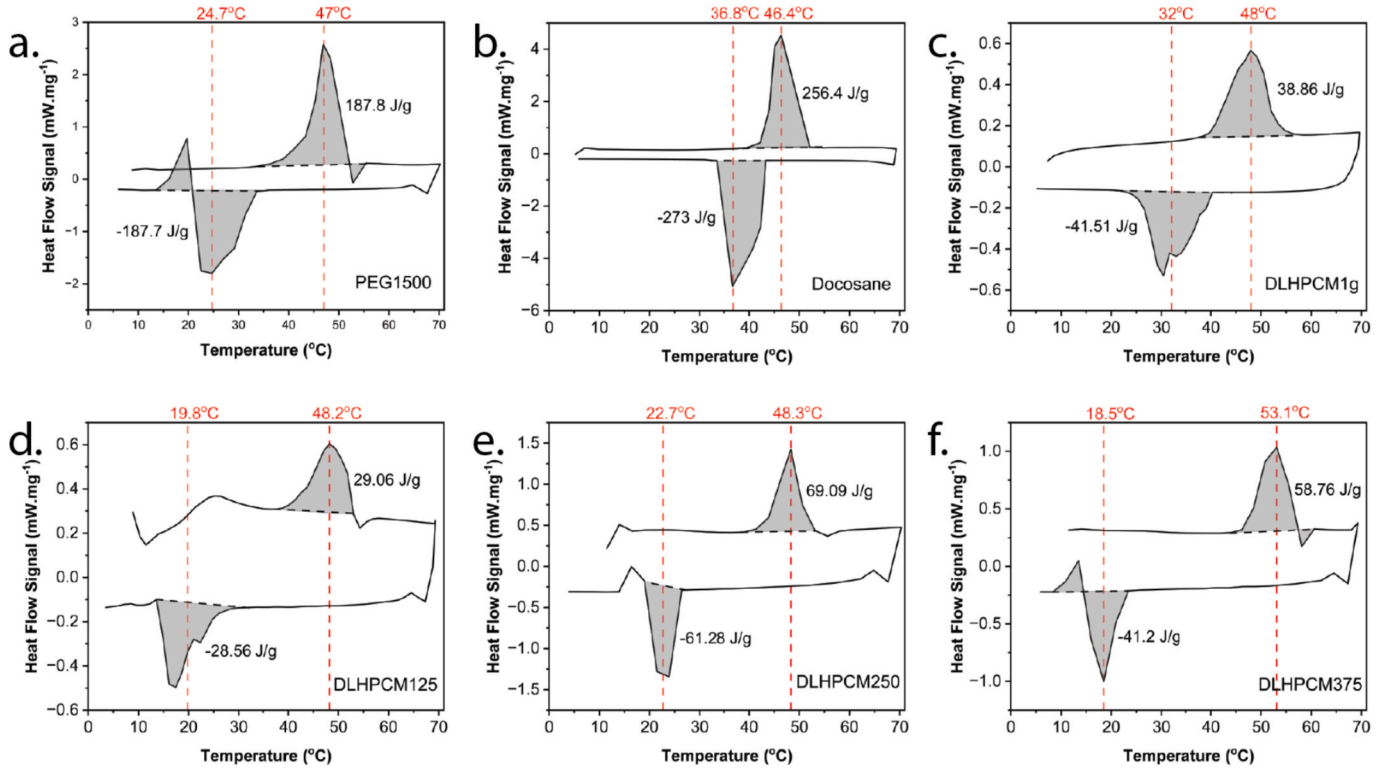

Fig. 4. Differential Scanning Calorimetry (DSC) charge discharge results of (a) PEG1500, (b) Docosane, (c) DLHPCM1g, (d) DLHPCM125, (e) DLHPCM250, and (f) DLHPCM375.

subjected to DSC analysis under a heating and cooling cycle between 5 and 70 °C, with a heating rate of 5 °C min^{-1}, to evaluate the heat charge/discharge behavior of the PCMs. As shown in Fig. 4**a and b**, PEG1500 exhibited a lower latent enthalpy for both charge and discharge processes compared to docosane. Notably, PEG1500′s demonstrated comparable latent enthalpy values during both charging and discharging. In contrast, docosane displayed a higher discharge latent enthalpy relative to its charge enthalpy, indicating a higher heat energy output. However, docosane discharges its stored latent enthalpy over a narrower temperature range, suggesting that PEG1500 retains heat for a longer duration despite its lower overall thermal energy output.

his charge/discharge behavior of PEG1500 and docosane was similarly observed in DLHPCM hydrogels, as shown in Fig. 4**c** – **f**. However, the encapsulation of both PCMs within the DLHs resulted in a reduction in latent enthalpy for both charge and discharge processes. This reduction can be attributed to several factors: the high hydrogel content relative to the encapsulated PCM, as well as bonding interactions between the PCMs and the hydrogel matrix. These factors likely create a thermal barrier that inhibits the heat storage and output capabilities of the PCMs. Additionally, the hydrogel structure confines the PCM molecules, restricting their molecular mobility and impeding their ability to undergo a complete phase transition, ultimately reducing their latent enthalpy [26].

Saturated DLH and DLHPCM hydrogels were then heated from 30 to 200 °C at a rate of 5 °C min^{-1} via DSC to examine and compare their water evaporation enthalpy characteristics with those of pure water, as shown in Fig. 5**a**. The result revealed distinct differences in the water evaporation process between the hydrogels and bulk water. The heat flow signal of water reached its maximum peak at roughly 100 °C, indicating complete water evaporation, followed by a sharp decline. In contrast, all hydrogels exhibited broader heat flow signal peaks compared to water. The DLHPCM-Docosane hydrogels displayed a slight reduction in the maximum evaporation enthalpy relative to water, indicating a decrease in evaporation enthalpy. In contrast, the DLHPCM-PEG1500 hydrogels exhibited the lowest evaporation enthalpy, followed by DLH, DLHPCM-Docosane and pure water (**Table S3**). In addition, the peak of the heat flow signal for all hydrogels shifted to a lower temperature range compared to pure water, suggesting that the water molecules within the hydrogels experienced early water release due to the presence of weak molecular interactions, known as intermediate water [1,2,27–29]. Importantly, the DSC analysis of the DLHPCM125 heat flow signal confirmed complete water evaporation, with an early water release peak at temperatures below 100 °C, followed by a higher temperature peak, indicative of the strong bonding of bound water molecules within the DLHPCM125 polymeric matrix.

The interactions of water molecule vibrational modes within their surrounding can be observed through the Gaussian sub-bands in the Raman spectral OH-region (2500 – 4000 cm^{-1}). These sub-bands can be differentiated into different donor (D) and acceptor (A) bonding species, including DAA-OH (2950 – 3100 cm^{-1}), DDAA-OH (3200 – 3350 cm^{-1}), DA-OH (3400 – 3500 cm^{-1}), and DDA-OH (3500 – 3600 cm^{-1}), with an additional free OH_2 sub-band (3600 – 3700 cm^{-1}) [30–32]. These vibrational stretching modes can be categorized into either strongly bonded free water (FW) containing DAA-OH and DDAA-OH vibrations, as well as weakly bonded intermediate water (IW) containing DA-OH and DDA-OH vibrations [33,34]. Weakly bonded IW molecules have a lower energy barrier, making them more susceptible to dissociation at finite temperatures. Their metastable nature promotes frequent proton exchanges with neighboring water molecules, forming H_3O^* units. This dynamic exchange weakens the hydrogen bonds, enabling IW to break free with minimal energy input and be released as small water clusters, which leads to faster water evaporation [2]. These modes are also present in the Raman spectra of DI water, DLH, and all DLHPCMs as shown in Fig. 5**b** — **i**. All hydrogels exhibited a higher IW:FW molar ratio compared to pure water, which facilitates a faster water evaporation rate as previously discussed. This observation also applies to DLHPCM-Docosane, further supporting the argument. Additionally, the IW:FW ratio results reflect the DSC evaporation enthalpy outcomes,

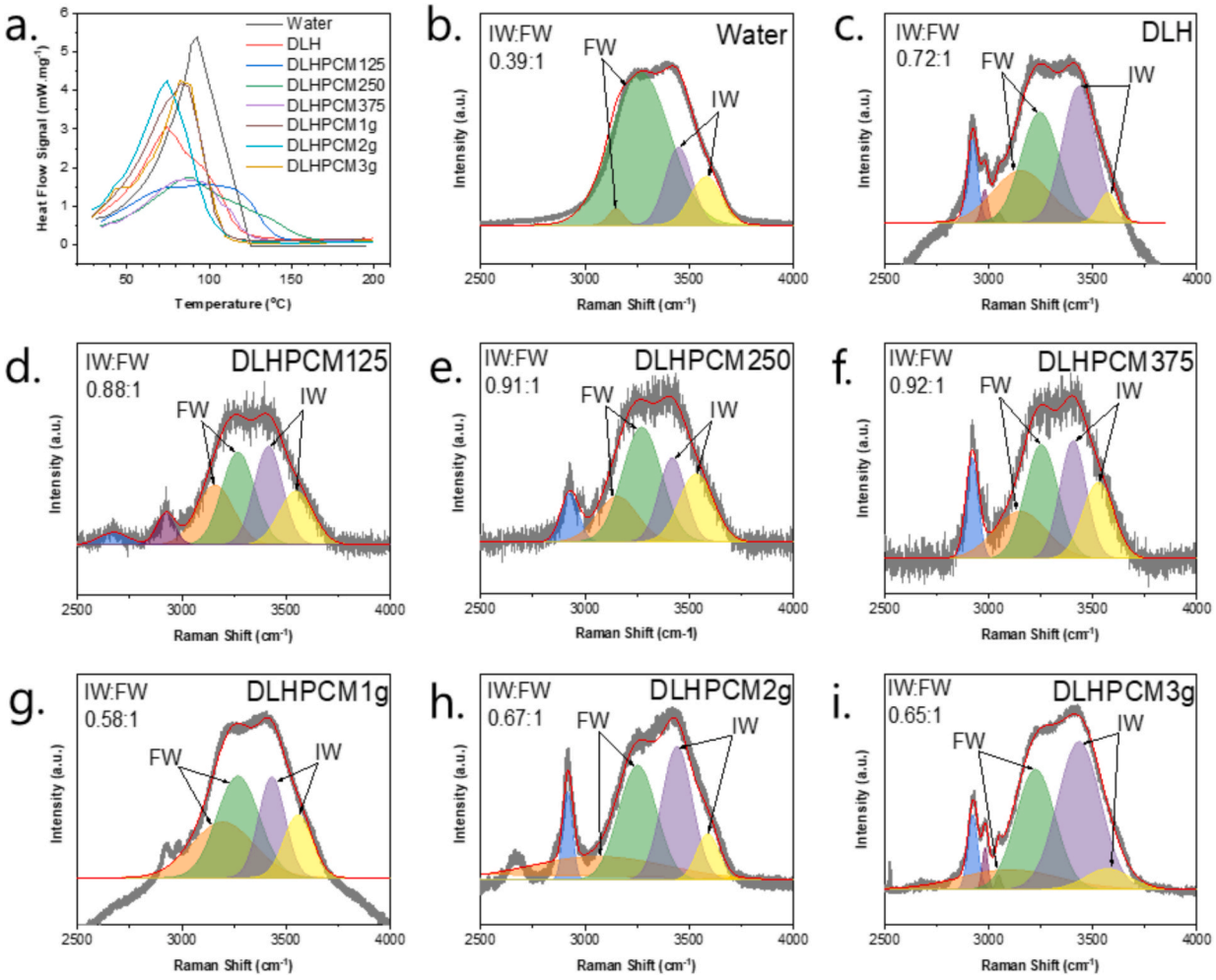

Fig. 5. Differential Scanning Calorimetry (DSC) analysis on water evaporation enthalpy of pure water and hydrogels. Raman spectra of (b) water, (c) DLH, (d-f) DLHPCM-PEG1500, and (g-i) DLHPCM-Docosane.

demonstrating the correlation of IW content to lowering the hydrogel's evaporation enthalpy.

3.2. Enhanced heat management

The frozen-dried samples of DLH and DLHPCMs were initially weighted to obtain their dehydrated mass. Each of the samples was then submerged within water to investigate each the water uptake rate. The mass was measured and recorded for every 5 min in an hour period to obtain its water absorption rate. To quantify the water evaporation performance of each hydrogel, solar steam generation (SSG) experiment was conducted using an in-house laboratory setting. As shown in Fig. 6**a, a** hydrogel sample was placed on a thermal insulating polystyrene (PS) foam to avoid any unnecessary water evaporation. A highly saturated tissue was wrapped on to the hydrogels to facilitate water transport for continuous water distillation (**Fig. S1**). The SSG process was initiated by a laboratory solar light simulator with an intensity of 1 kW m^{-2} (one sun irradiation). This setup was placed on top of a polyethylene (PE) foam to avoid any heat conduction from the mass balance base plate. The surface temperatures of all samples were determined via IR measurements. Mass loss was then recorded sequentially to determine each hydrogel's evaporation performance. Water evaporation under light exposure was conducted for 60 min, after which the light source was turned off. Subsequently, water evaporation was measured in the dark for 20 min to assess and compare the heat storage performance of each phase change material (PCM).

As shown in Fig. 6b, increasing the concentration of docosane significantly boosts heat generation rates in DLHPCM-Docosane hydrogels. However, further increasing the concentration from 2 g to 3 g appears to yield no additional improvement in heat generation. In contrast, within the DLHPCM-PEG1500 hydrogels, increasing crosslinking density allows the hydrogel to generate heat at a faster rate. This is because heat conduction primarily occurs through nonbonding (van der Waals) interactions and covalent bonding. Higher crosslinking density reduces the polymer interchain distance, therefore increasing the rate of heat conduction [35]. Specifically, the incorporation of hydrophobic PCM significantly increased the surface temperature of the DLHPCM-Docosane samples to 60–65 °C, compared to the surface temperatures of DLHPCM125 to DLHPCM375, which were ~ 48 °C (Fig. 6**b**). Nevertheless, the surface temperatures of all DLHPCM samples exceeded that of the control DLH, which remained below 40 °C after one hour irradiation. When light exposure was blocked, all DLHPCM hydrogels retained relatively high surface temperatures after 1 h, with DLHPCM-3 g achieving the highest temperature at 27 °C. This indicates that the PCMs effectively released stored heat for continued utilization.

As shown in Fig. 6**c**, DLHPCM375 achieved the highest water evaporation rate of 3.52 kg $m^{-2}h^{-1}$ compared to pure water, the DLH control, and other DLHPCMs. This is primarily because it increases the IW content, lowers the evaporation enthalpy of water, and optimizes the surface temperature, facilitating rapid water evaporation. The DLHPCM375 hydrogel outperformed the DLH and other DLHPCMs by achieving higher dark water evaporation when the light source was removed, with

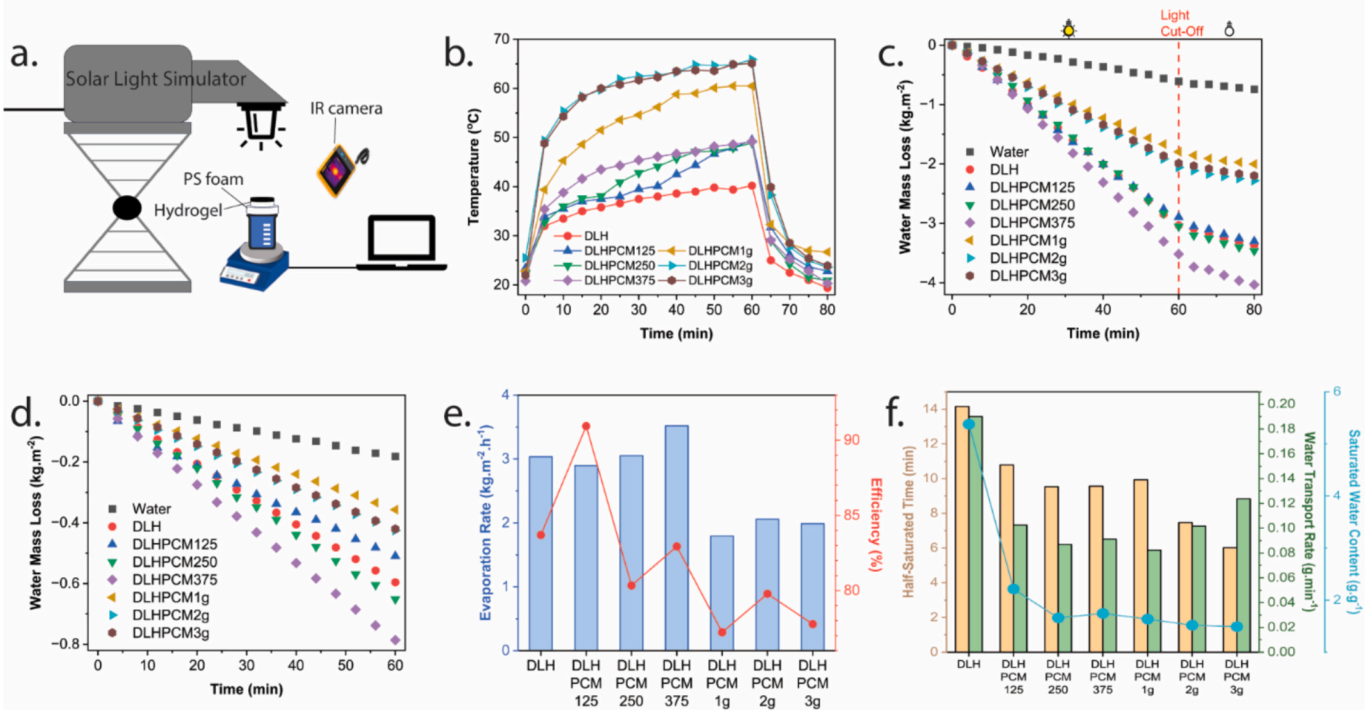

Fig. 6. (a) Schematic diagram of water evaporation test setup. (b) Saturated hydrogels' surface temperature throughout water evaporation test exposed under 1 sun ($\leq$1 kW.m^{-2}). (c) Light and (d) dark water evaporation rate performance of water, DLHPCM-PEG1500, and DLHPCM-Docosane hydrogels. (e) Water evaporation performance and efficiency summary of all hydrogels. (f) Summary of water transport rate of hydrogels.

an additional 0.51 kg m^{-2} of water evaporated over a 20-minute period which is 35 % and 75 % higher compared to DLH and pure water, respectively. Despite the good water evaporation performance of the DLH under sunlight, the DLHPCM125 and DLHPCM250 demonstrated faster water evaporation rates during light-cutoff conditions, as summarized in **Table S1**. These findings demonstrate that incorporating PCM materials into the SSG systems not only raises the evaporation surface temperature but also stores excess heat, enabling water evaporation even in the absence of sunlight. Additionally, **Table S2** presents the evaporation rates following irradiation shutdown for state-of-the-art PCM-containing SSG systems. The DLHPCM375 hydrogel stands out, achieving the highest surface temperature of 48 °C and an evaporation rate of 26 g m^{-2} min^{-1} among 2D evaporators, which is comparable to the evaporation rate of the 3D hydrogel/ fiber evaporator with solid–solid phase change materials (SPCM).

As shown in Fig. 6**d**, we further investigated the dark water evaporation properties of all the hydrogels and found that DLHPCM375 exhibited the highest dark evaporation rate. This superior performance was attributed to the encapsulated PCM PEG1500, which contains a greater number of hydrophilic functional groups. These groups increased the IW content and significantly reduced the enthalpy of evaporation (refer to previously discussion and shown in Fig. 5**b** – **i)**.

It is important to note that the enthalpy of evaporation obtained from DSC measurements differs from the theoretical enthalpy of evaporation derived from dark water evaporation. This discrepancy arises because, in DSC testing, the saturated hydrogel undergoes complete dehydration, whereas only partial evaporation occurs during the dark water evaporation process. Consequently, the hydrogel's theoretical evaporation enthalpies are lower than the value determined by DSC.

The theoretical enthalpy can be thermodynamically determined through the water and hydrogels dark water evaporation rate as shown in **Eq.** (1).

$$U_{in} = \dot{m}_w \Delta H_w = \dot{m}_h \Delta H_{vap} \quad (1)$$

where ΔH_w represents the bulk water theoretical evaporation enthalpy ΔH_{vap} denotes the evaporator's equivalent evaporation enthalpy, $\dot{m}_w$ is the mass change of bulk water, and $\dot{m}_h$ is the hydrogel's water mass change [1,2,29,36].

Both DLHPCM-PEG1500 and DLHPCM-Docosane showed the same enthalpy trend for both DSC obtained and theoretical value. DLH and DLHPCM125 theoretical enthalpy demonstrated the opposite effect compared to their obtain DSC enthalpy. This explains why DLH would have a higher dark water evaporation rate than DLHPCM125. This phenomenon is caused by the reduction of DLHPCM125 water saturated content and transport rate caused by the PCM encapsulation. This is demonstrated by the first 25 min of DLH and DLHPCM125 similar dark water evaporation performance. The similarity in performance indicated that DLHPCM125's low evaporation enthalpy effectively offsets DLH's high saturated water content and transport rate. However, due to DLHPCM125 low water absorption rate, DLH outperforms it within the remainder of the 1-hour continuous distillation period.

The water evaporation performance efficiency of each hydrogel can be determined as shown in **Eq.** (2).

$$\eta = \frac{\dot{m}_h (C_p \Delta T + \Delta H_{vap})}{c_{opt} I A \Delta t} \quad (2)$$

where C_p is the specific heat capacity of water (4.18 kJ kg^{-1} K^{-1}), ΔT is the liquid temperature change, c_{opt} is the optical concentration, I is the solar irradiation, A is the evaporator's exposed surface area and Δt is the evaporation period [1,2,29,36].

Fig. 6**e** highlights the water evaporation rate and efficiency summary of DLH and each DLHPCM hydrogel. Among the DLHPCM-PEG1500, it appears that increasing the crosslinking density seems to increase the water evaporation rate. As mentioned, DLHPCM375 showed the highest water evaporation rate, followed by DLHPCM250 and DLH. Despite its fast evaporation rate, DLHPCM375 and DLH showed relatively lower efficiencies of 83 % compared to DLHPCM125, which had the highest efficiency at 91 %, and DLHPCM250, which displayed the lowest efficiency at 80 %. The reduced efficiency of DLHPCM375 can be attributed to its high surface evaporation temperature and low evaporation

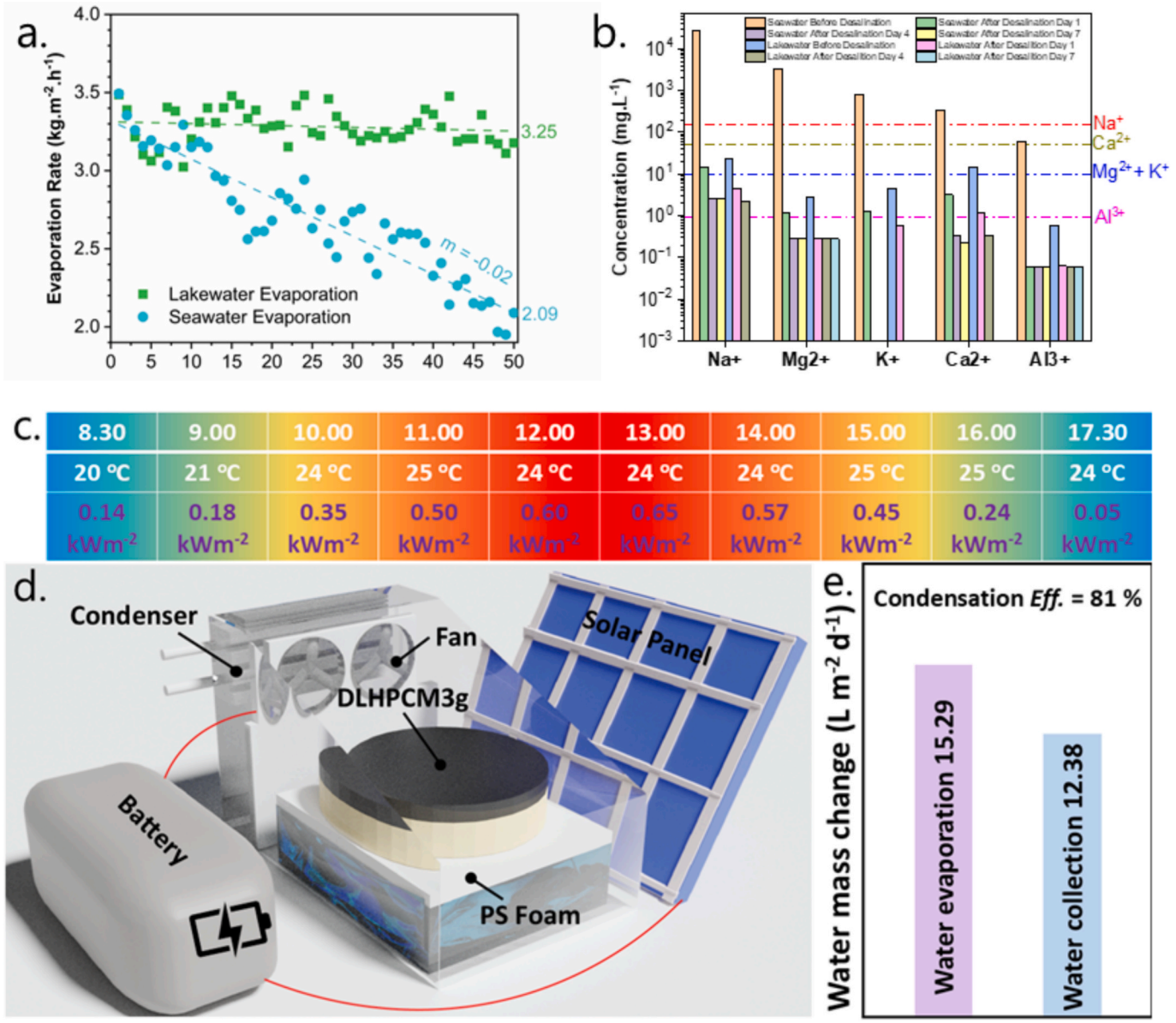

Fig. 7. Desalination/lake-water filtration SSG indoor testing: (a) Evaporation rates of DLHPCM375 over 50 cycles test in lake water and seawater water distillation tests. (b) The ionic concentrations of the collected clean water. Up-scale DLHPCM375 outdoor testing. (c) Weather condition throughout the day. (d) Schematic prototype SSG device. (e) Water evaporation and collection results.

enthalpy, which promote rapid water release. However, its limited saturation capacity and insufficient water absorption rate, as shown in Fig. 6**f**, hinder water replenishment within the hydrogel, thereby decreasing its overall efficiency. In contrast, DLH, with its lower surface temperature and higher evaporation enthalpy, possesses a high saturation capacity and water absorption rate, ensuring sufficient water replenishment for evaporation. Nevertheless, its inefficiency is likely due to oversaturation, which results in heat loss and higher evaporation enthalpy, negatively impacting its performance. Meanwhile, DLHPCM125 achieves an optimal balance of water absorption, heat generation, and water absorption. This combination enables a favorable surface temperature, evaporation enthalpy, and sufficient replenishment, resulting in the highest efficiency despite its slower evaporation rate. On the other hand, DLHPCM250, while having a water absorption rate similar to DLHPCM375, generates heat a slower rate, which contributes to its comparatively lower efficiency among the DLHCPM-PEG1500 hydrogels.

For DLHPCM-Docosane, the water evaporation performance of all hydrogels significantly decreased, showing low evaporation efficiency despite achieving very high surface temperatures. This decline is primarily attributed to the incorporation of hydrophobic docosane. As confirmed by the FTIR results discussed earlier, the presence of docosane reduces the abundance of hydrophilic functional groups, thereby increasing evaporation enthalpy. Additionally, its hydrophobic nature limits the hydrogel's water absorption capacity, resulting in inadequate water replenishment and further diminishing evaporation efficiency.

Hydrogel's water absorption rate can be measured by their water transport rate (V), half-saturation time (t), and saturated water content (Q) as shown in **Eq.** (3) and **Eq.** (4).

$$Q = W/W_{dry} \tag{3}$$

$$V = 0.5Q_s/t \tag{4}$$

where W/W_{dry} is the ratio between the saturated and dry state of the hydrogel and $0.5Q_s$ is the hydrogel's half-saturated state.

As shown in Fig. 6**f**, the addition of PCMs to DLHs reduces their water

absorption capacity. This reduction is primarily due to PCM encapsulation, which limits the hydrogel swelling capacity. PCM remains in a solid state at room temperature, obstructing the micro/macro-porous structure as previously shown by the SEM cross-sectional images. For DLHPCM-PEG1500 hydrogels, water absorption rates decrease with increasing crosslinking density. Conversely, in DLHPCM-Docsoane hydrogels, a higher concentration of docosane reduced the hydrogel's half-saturation time while increasing its water transport rate. This increase in water transport rate may be attributed to the formation of a thin water film on the hydrophilic/hydrophobic polymeric matrix surface within the hydrogel [37]. The thin water film likely contributes to the reduced half-saturation time, as it evaporates before fully saturating the hydrogel. Despite this, DLHPCM-Docosane does not exhibit a low evaporation enthalpy, indicating that the presence of a thin water film does not necessarily promote rapid water evaporation process. Instead, the presence of hydrophilic functional groups remains the most critical factor for forming IW, which is essential for efficient water release/evaporation.

3.3. Solar steam generation applications

DLHPCM375, which demonstrated the highest water evaporation rate, was tested for its stability and filtration capability by consecutively filtering DI water, seawater, and lake-water, obtained within the local coastal and creek area of Sydney. Similar to the indoor SSG setup, the hydrogel was wrapped with a water absorbing tissue and placed on a PS foam positioned on the surface of DI water, seawater, or lake-water. DLHPCM375 demonstrates stable evaporation and thermal performance, maintaining consistency through 30 DI water evaporation cycles of continuous heating and cooling before washing, with no observed decline in maximum surface temperature and heat retention property (**Fig. S3**). The system was then placed inside a sealed glass container to capture condensed vapor, which was subsequently analyzed via ICP-MS, as shown in Fig. 7. The desalination and lake-water evaporation stability tests consisted of 50 evaporation cycles, each lasting 1 h and an average evaporation rate was recorded. The results showed no salt accumulation or hydrogel fouling (**Fig. S2**), quantitatively demonstrating effective salt and bacterial rejection, as well as long-term stability and reusability.

The desalination and lake-water evaporation stability tests consisted of 50 evaporation cycles, each lasting 1 h with the average evaporation rate recorded for each cycle. As Illustrated in Fig. 7**a**, DLHPCM375 maintained a high and stable evaporation rate in lake-water, with only a slight decline to 3.25 kg $m^{-2}h^{-1}$ over the test cycles. In contrast, its performance during desalination exhibited a gradual decrease of approximately 0.02 kg $m^{-2}h^{-1}$ per cycle. This decline is attributed to the electrostatic attractions between the cation groups of PAETAC and the salt ions, which led to hydrogel shrinkage during the desalination process [38]. Nevertheless, this effect can be mitigated by rinsing in fresh water. Seawater and lake-water vapor samples were collected on days 1, 3, and 7. Standard solutions containing various metal ions were analyzed using ICP-MS to detect metal ions in the collected samples. As shown in Fig. 7**b**, five metal ions (Na^+, Mg^{2+}, K^+, Ca^{2+}, and Al^{3+}) were identified in the seawater and lake-water used for filtration testing of DLHPCM375. The filtration results demonstrated that DLHPCM375 effectively reduced the concentration of these metal ions over time, with levels decreasing consistently across the testing period. The metal ions concentration of the filtered seawater and lake-water were detected to be below the WHO drinking water standards [39–42].

The scaled-up outdoor water evaporation test was conducted in an open field under real-world conditions. Outdoor temperature and varying solar intensity were recorded (Fig. 7**c**). As shown in Fig. 7**d**, the setup included a water-cooling condenser and a fan powered by an external outlet connected to a solar panel, which remained exposed to sunlight throughout the day. The condenser and fan worked together to accelerate vapor condensation, resulting in a higher freshwater yield. Despite relatively low sunlight intensity (average solar intensity = 0.44 kW m^{-2}), DLHPCM375 achieved a remarkable freshwater yield of 12.4 L m^{-2} day^{-1} or 13.10 L kWh^{-1}, with an impressive condensation efficiency exceeding 80 % (Fig. 7**e**). The estimated material and production cost were at \$47.72 m^{-2} and \$3.98 L^{-1} day^{-1} respectively.

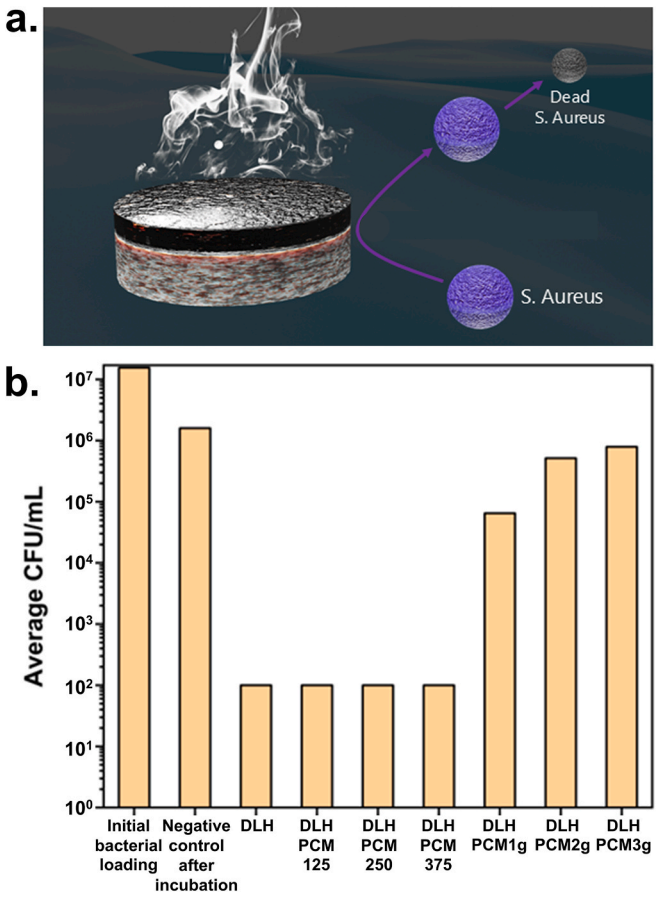

Fig. 8. (a) DLHPCM-PEG1500's anti-bacterial mechanism illustration. (b) S. Aureus colony-forming unit (CFU) results of DLH and DLHPCM hydrogels.

The Gram-positive pathogenic bacteria *Staphylococcus. aureus* is commonly found in food products and environmental water samples [43,44]. To evaluate antibacterial properties, this bacteria strain was exposed to DLH and all DLHPCM hydrogels and incubated for 24 h. As shown in Fig. 8, hydrophilic hydrogels such as DLH and DLHPCM-PEG1500 eliminated 99.99 % of *S. aureus*, likely due to the entrapment of the bacteria by the cationic PAETAC in the hydrogels that eventually led to cell death [45,46]. In contrast, DLHPCM-Docosane hydrogels only partially reduced bacterial activity, with higher docosane concentrations worsening antibacterial performance. This suggests that incorporating hydrophobic materials may not necessarily result in better antimicrobial performance (especially against Gram-positive pathogens), as certain bacteria can degrade n-alkanes and aromatic hydrocarbons, either enzymatically or through other metabolic pathways to generate energy and sustain bacterial growth [47–49].

4. Conclusion

In this study, we developed a novel DLH structure incorporating hydrophobic or hydrophilic PCM to address the thermal instability of SSGs under intermittent sunlight exposure. While PCM encapsulation partially clogs the hydrogel pores, reducing the water absorption capacity of DLHPCM, the introduction of hydrophilic PCM in the DLHPCM-PEG1500 hydrogel offsets this limitation by increasing the IW content, thereby lowering the enthalpy of water evaporation. The resulting DLHPCM375 demonstrates superior thermal management,

achieving a rapid water evaporation rate of 3.52 kg $m^{-2}h^{-1}$ with an efficiency of 83 %. Its cationic functional groups effectively re-dissolve salts formed during desalination into the saline source and entraps and kills Gram-positive bacteria. Outdoor testing under fluctuating weather conditions confirmed the system's robustness, with the scale-up DLHPCM375 producing a freshwater yield of 12.4 L m^{-2} day^{-1}. All in all, the capacity of DLHPCM to mitigate thermal instability under varying solar irradiance offers a promising pathway for the practical implementation of SSG technology.

CRediT authorship contribution statement

Casey Onggowarsito: Writing – original draft, Validation, Methodology, Investigation, Data curation, Conceptualization. **Stella Zhang:** Data curation. **Yihan Shi:** Data curation. **Shudi Mao:** Validation, Data curation. **An Feng:** Data curation. **Gabriela Martins:** Resources. **Zeyu Shao:** Resources, Data curation. **Edgar H.H. Wong:** Resources, Investigation, Data curation. **Wenshan Guo:** Writing – review & editing, Resources. **Qiang Fu:** Writing – review & editing, Supervision, Methodology, Funding acquisition, Conceptualization.

Declaration of competing interest

The authors declare that they have no known competing financial interests or personal relationships that could have appeared to influence the work reported in this paper.

Acknowledgement

Q. Fu acknowledges the financial support from the Australian Research Council (FT180100312).

Appendix A. Supplementary data

Supplementary data to this article can be found online at https://doi.org/10.1016/j.cej.2025.162838.

Data availability

Data will be made available on request.

References

[1] C. Onggowarsito, et al., *Water Harvesting Strategies through Solar Steam Generator Systems*, ChemSusChem 15 (23) (2022) e202201543.
[2] C. Onggowarsito, et al., *Updated perspective on solar steam generation application*, Energ. Environ. Sci. 17 (6) (2024) 2088–2099.
[3] R. Yalamanchili, et al., *Can a forward osmosis-reverse osmosis hybrid system achieve 90 % wastewater recovery and desalination energy below 1 kWh/m3? A Design and Simulation Study*. Desalination 585 (2024) 117767.
[4] C. Onggowarsito, et al., *Development of an innovative MnO2 nanorod for efficient solar vapor generator*, Environmental Functional Materials 1 (2) (2022) 196–203.
[5] J. Pan, et al., *Victoria amazonica-inspired sandwich-structure interfacial solar steam generator*, Chem. Eng. J. 492 (2024) 152305.
[6] X. Zhang, et al., *Dealloying-Derived Self-Supporting Nanoporous Zinc Film with Optimized Macro/Microstructure for High-Performance Solar Steam Generation*, ACS Appl. Mater. Interfaces 16 (18) (2024) 23141–23149.
[7] S.N. Farabi, et al., *The future of solar-driven interfacial steam generation for sustainable water desalination: Drivers, challenges, and opportunities-review*, Results Eng. 23 (2024) 102649.
[8] A. Gnanasekaran, K. Rajaram, *Rational design of different interfacial evaporators for solar steam generation: Recent development, fabrication, challenges and applications*, Renew. Sustain. Energy Rev. 192 (2024) 114202.
[9] P. Zhang, et al., *Boosting the Viable Water Harvesting in Solar Vapor Generation: From Interfacial Engineering to Devices Design*, Adv. Mater. 36 (5) (2024).
[10] M. Shafaee, E.K. Goharshadi, H. Behnejad, *Salt-resistant hierarchically porous wood sponge coated with graphene flake/polyaniline nanocomposite for interfacial solar steam production and wastewater treatment*, Sol. Energy 276 (2024) 112707.
[11] L. Sun, et al., *Ultra-high solar steam generation based on regulated water management strategy in 3D biomass hydrogels inspired by the "binding effect" of cell walls*, Desalination 587 (2024) 117954.
[12] H. Li, et al., *Thermoresponsive Janus hybrid hydrogel for efficient solar steam generation*, Nano Energy 124 (2024) 109475.
[13] X. Dai, et al., *Apple leaf-inspired bilayered Janus wood evaporator with decoupled light-vapor interfaces for high-efficiency solar steam generation*, Chem. Eng. J. 499 (2024) 155796.
[14] I. Ait Laasri, et al., *Recent progress, limitations, and future directions of macro-encapsulated phase change materials for building applications*, Renew. Sustain. Energy Rev. 199 (2024) 114481.
[15] H. Wang, et al., *Investigation of the thermal management potential of phase change material for lithium-ion battery*, Appl. Therm. Eng. 236 (2024) 121590.
[16] Muthukumar, P. and H. Niyas, Materials, Design and Development of Latent Heat Storage Systems for Medium and Large-Scale Applications: Issues and Challenges, in Encyclopedia of Renewable and Sustainable Materials, S. Hashmi and I.A. Choudhury, Editors. 2020, Elsevier: Oxford. p. 417-437.
[17] Nicholas, A.F., et al., *Chapter 12 - Activated Carbon for Shape-Stabilized Phase Change Material*, in *Synthesis, Technology and Applications of Carbon Nanomaterials*, S.A. Rashid, R.N.I. Raja Othman, and M.Z. Hussein, Editors. 2019, Elsevier. p. 279-308.
[18] A. Palacios, et al., *A perspective on Phase Change Material encapsulation: Guidance for encapsulation design methodology from low to high-temperature thermal energy storage applications*, J. Storage Mater. 72 (2023) 108597.
[19] K. Abdel Tawab, M.M. Magida, S.M. Ibrahim, *Effect of Ionizing Radiation on the Morphological, Thermal and Mechanical Properties of Polyvinyl Alcohol/Polyethylene Glycol Blends*, J. Polym. Environ. 19 (2) (2011) 440–446.
[20] S.A. Nouh, K. Benthami, M.M. Abutalib, *Modification of structural and optical properties of polyvinyl alcohol/polyethylene glycol thin film by laser irradiation*, Radiat Eff. Defects Solids 171 (1–2) (2016) 87–95.
[21] A. Onder, et al., *Removal of dye from aqueous medium with pH-sensitive poly[(2-(acryloyloxy)ethyl]trimethylammonium chloride-co-1-vinyl-2-pyrrolidone] cationic hydrogel*, J. Environ. Chem. Eng. 8 (5) (2020) 104436.
[22] I. Deleanu, et al., *Potassium sorbate release from poly(vinyl alcohol)–bacterial cellulose films*, Chem. Pap. 66 (2012) 138–143.
[23] Sudesh, et al., *Effect of graphene oxide doping on superconducting properties of bulk MgB2*. Superconductor Science and Technology, 2013. **26**(9): p. 095008.
[24] P. Felix De Castro, D.G. Shchukin, *New Polyurethane/Docosane Microcapsules as Phase-Change Materials for Thermal Energy Storage*. Chemistry – A, European Journal 21 (31) (2015) 11174–11179.
[25] A. Dabbagh, et al., *Polyethylene glycol-coated porous magnetic nanoparticles for targeted delivery of chemotherapeutics under magnetic hyperthermia condition*, Int. J. Hyperth. 36 (1) (2019) 104–114.
[26] H. Zhang, et al., *Super-elastic smart phase change material (SPCM) for thermal energy storage*, Chem. Eng. J. 411 (2021) 128482.
[27] S. Mao, et al., *A cryogel solar vapor generator with rapid water replenishment and high intermediate water content for seawater desalination*, J. Mater. Chem. A 11 (2) (2023) 858–867.
[28] X.S. Zhang, et al., *Boron nanosheets boosting solar thermal water evaporation*, Nanoscale 16 (9) (2024) 4628–4636.
[29] Y. Shi, et al., *Hydrogels in solar-driven water and energy production: Recent advances and future perspectives*, Chem. Eng. J. 492 (2024) 152303.
[30] S.W. Wakolo, et al., *Various states of water species in an anion exchange membrane characterized by Raman spectroscopy under controlled temperature and humidity*, PCCP 26 (3) (2024) 1658–1670.
[31] S.W. Wakolo, et al., *Coherent anti-Stokes Raman scattering spectroscopy system for observation of water molecules in anion exchange membrane*, Spectrochim. Acta A Mol. Biomol. Spectrosc. 309 (2024) 123875.
[32] Q. Sun, *The Raman OH stretching bands of liquid water*, Vib. Spectrosc 51 (2) (2009) 213–217.
[33] C. Li, et al., *A Covalent Organic Framework/Graphene Dual-Region Hydrogel for Enhanced Solar-Driven Water Generation*, J. Am. Chem. Soc. 144 (7) (2022) 3083–3090.
[34] X. Geng, P. Yang, Y. Wan, *How to reduce enthalpy in the interfacial solar water generation system for enhancing efficiency?* Nano Energy 123 (2024) 109434.
[35] V. Rashidi, et al., *Thermal Conductance in Cross-linked Polymers: Effects of Non-Bonding Interactions*, J. Phys. Chem. B 121 (17) (2017) 4600–4609.
[36] S. Mao, et al., *Recent developments of hydrogel based solar water purification technology*, Mater. Adv. 3 (3) (2022) 1322–1340.
[37] Z. Yu, et al., *Micro–Nano Water Film Enabled High-Performance Interfacial Solar Evaporation*, Nano-Micro Letters 15 (1) (2023) 214.
[38] C.-J. Lee, et al., *Ionic Conductivity of Polyelectrolyte Hydrogels*, ACS Appl. Mater. Interfaces 10 (6) (2018) 5845–5852.
[39] World Health, O. *Sodium in Drinking-water*. 2003; Available from: https://www.who.int/water_sanitation_health/dwq/chemicals/sodium.pdf.
[40] Edition, F., *Guidelines for drinking-water quality*. WHO chronicle, 2011. **38**(4): p. 104-8.
[41] World Health, O., *Calcium and magnesium in drinking water : public health significance*. 2009, World Health Organization: Geneva.
[42] World Health, O., Potassium in drinking-water : background document for development of WHO guidelines for drinking-water quality. 2009, World Health Organization: Geneva.
[43] I. Ofori, et al., *Chlorine dioxide inactivation of Pseudomonas aeruginosa and Staphylococcus aureus in water: The kinetics and mechanism*, J. Water Process Eng. 26 (2018) 46–54.
[44] M. Zhang, et al., *Effects of citronellal on growth and enterotoxins production in Staphylococcus aureus ATCC 29213*, Toxicon 213 (2022) 92–98.
[45] A. Kumar, et al., *Highly Bactericidal Macroporous Antimicrobial Polymeric Gel for Point-of-Use Water Disinfection*, Sci. Rep. 8 (1) (2018) 7965.
[46] E. Wulandari, et al., *Silk Sponges with Surface Antimicrobial Activity*, ACS Appl. Bio Mater. 4 (1) (2021) 692–700.

[47] X. Hu, et al., *N-alkane shape distinctive microbial patterns in Kuroshio Extension*, Environ. Int. 188 (2024) 108757.
[48] J. Brzeszcz, et al., *Bacteria degrading both n-alkanes and aromatic hydrocarbons are prevalent in soils*, Environ. Sci. Pollut. Res. 31 (4) (2024) 5668–5683.
[49] B. Hussain, et al., *Niche-specific modulation of long-chain n-alkanes degrading bacterial community and their functionality in forest habitats across the leaf litter-soil compartments*, Appl. Soil Ecol. 195 (2024) 105248.